High throughput quantitative tracking of single parasite in *Plasmodium falciparum*

Zhe Cheng[*1,2], Liyang Ru[5], Andrew Hoang[2], Mingyu Wang[4], Suryanarayana Ganjikunta[2], Steven P. Maher[1], Dennis E. Kyle[*1,2,3]

1. Center for Tropical and Emerging Global Disease, University of Georgia, Athens, GA, USA
2. Department of Cellular Biology, University of Georgia, Athens, GA, USA
3. Department of Infectious Disease, University of Georgia, Athens, GA, USA
4. Department of Bioinformatics, University of Georgia, Athens, GA, USA
5. Department of Electrical Computer and Engineering, University of Florida, Gainesville, FL, USA

*Corresponding authors: Dennis.Kyle@uga.edu and Zhe.Cheng@uga.edu

Abstract

New systematic profiling of drug effects is in urgent demand due to limitations in existing drug assessment approaches to evaluate comprehensive drug effects and distinguish heterogeneity in mixed populations. One challenge is the underdeveloped methods for investigation of causal association between artemisinin induced dormancy and recrudescence in *Plasmodium falciparum*. We developed Quantitative Tracking After Chemotherapy Exposure (qTRACE) and its artificial intelligence (AI) mode to evaluate cytotoxic and cytostatic effects simultaneously from single parasite resolution in a high throughput manner. Applying qTRACE, we revealed true parasite-drug killing dynamics after artemisinin exposure and found that up to 50% of viable parasites originate from recovery of artemisinin-induced dormancy. We further developed next generation qTRACE integrated with deep learning-based segmentation and analysis, thereby directly linking time-lapse phenotypes of label-free live cell. qTRACE is a versatile platform for in-depth single cell level drug effects evaluation, recovery after drug exposure studies and complex long-term growth experiments.

45 **Introduction**

46 Accurate evaluation of drug induced effects and parasite viability is essential for
47 discovering new anti-malarial medicines and monitoring the success of current regimen of
48 treatments. Previously, evaluation of susceptibility to anti-malarial drugs typically are measured
49 by half-maximal inhibitory concentration (IC50) or various ring stage survival assays[1-5]. These
50 assays are carried out in a bulk culture for short periods of time; susceptibility of drugs is
51 measured by comparing the number of replicated parasites between treated and untreated
52 condition in a mixed culture. Many of these methods rely on taking aliquots from a large culture
53 and only capture a single snapshot. Drug perturbation assessments often lack insights into drug
54 effects and confuse growth inhibition and temporary arrest with killing. More critical limitations
55 are the inability to evaluate long-term drug-parasite dynamics as the measurements are not
56 derived from the same cells and cannot resolve heterogeneity in a mixed population. Too often
57 the result is misinterpreted as killing rate or that no viable parasites remain in the assay when
58 many persisted survivors exist, therefore obscuring true killing effects of drugs and hindering the
59 development of next generation anti-malarial medicines. Consequently, these methods create
60 inconsistent correlation between drug susceptibility and genotypes, while ignoring valuable
61 biological insights of individual diversity of parasites and drug effects in a continuous system.

62 Artemisinin combination therapy is the frontline treatment for *Plasmodium falciparum*
63 infection. However, the emergence and spread of resistance to artemisinin has posed a
64 significant threat in malaria control[6]. Delayed clearance and recrudescence are frequently
65 associated with artemisinin resistance clinically[7]. It has been widely reported that exposure to
66 artemisinin drugs induce a phenotype known as artemisinin induced dormancy and these
67 dormant parasites can persist for many days before they either recover or die. Numerous
68 studies suggest these dormant parasites play a role in infection recrudescence and treatment
69 failures both in clinic and in vitro[8-12]. Drug-induced cell cycle arrest has been widely observed in

70 many human diseases, including malaria, and have posed a significant challenge in searching
71 for improved therapies[13]. Thus, understanding the interaction of dormancy with artemisinin
72 resistance and parasite recrudescence is critical for formulating effective counterstrategies.
73 However, the causal relation of artemisinin induced dormancy to parasite survival and
74 recrudescence remains poorly understood due to limitations in existing approaches. Some of
75 the variant assays attempted to compensate for delayed recovery and quantify dormancy
76 recovery, but still facing the same flaw that early survivors can easily disguise the existence of
77 recovered parasites in a mixed culture[2, 14]. There is a demand for improved and more efficient
78 evaluation of artemisinin effects and artemisinin induced dormancy to address global drug
79 resistance of malaria infection.

80 In this study, we developed Quantitative Tracking After Chemotherapy Exposure
81 (qTRACE) to quantify viability and growth at single parasite resolution based on the concept that
82 with significant dilution of parasitized erythrocytes, one parasite grows into a colony that can be
83 visualized microscopically. qTRACE is a versatile method that simultaneously tracks survival,
84 time-dependent recovery, and drug-induced growth effects. We show the robustness of
85 qTRACE by revealing true long-term drug effects of dihydroartemisinin (DHA) on multiple *P.*
86 *falciparum* isolates and cloned parasites with diverse backgrounds. We further clarify the
87 underappreciated contribution of artemisinin induced dormancy in parasite recrudescence that
88 cannot be properly measured before. For the first time, we reveal the undiscovered growth
89 retardation effect of artemisinin drugs in selected parasite strains. Further development of
90 qTRACE AI with deep learning-based cellular analysis effectively enhanced time-lapse
91 biological connection, generalization, and accuracy through unrestricted observation of label-
92 free live cell phenotypes. Applying qTRACE in drug testing, we found a diverse cytostatic and
93 cytotoxic effect preference and time-dependent dynamics between drugs and parasites.

qTRACE is strongly positioned for holistic understanding of single cell level drug-parasite dynamics and easy access to intricate experiments.

114 **Results**

115 **Quantification of longitudinal viability and growth of single parasite**

116 We found that, with diluted parasite seeding density, one single parasite grows into a
117 colony and can be continuously monitored over time. These initial observations led us to
118 develop a high throughput and high content imaging assay. Single digit GFP integrated
119 parasites (NF54-GFP) were seeded into 384 well plate and imaged continuously using a 4x
120 objective on a high content imaging system (HCI). In these assays we observed continuous
121 formation and growth of colonies over 22 days (Fig. 1A). Day 5 was the earliest time we could
122 detect a colony, presumably because the number of parasites in a colony prior to day 5 did not
123 produce enough fluorescence intensity at low magnification to be differentiated from
124 background. These colonies continued to grow at the same position in the well throughout the
125 duration of the assay (22 days) (Fig. 1A). Meanwhile, we also observed parasite recovery and
126 colony growth in parasites exposed to 700nM DHA for 6h (Fig. 1A). Notably, some colonies
127 appeared at later timepoints, which is consistent with the concept that artemisinin drugs induce
128 ring stage dormancy, followed by delayed recovery of the parasites (Fig. 1A). Time-lapse video
129 of high content imaging data showed the differential onset of growth of individual parasites and
130 that late recovering parasite colonies from dormancy were detected in the same well as early
131 recovering parasites (Supplementary Video 1). Comparison of GFP, Hoechst, and DIC imaging
132 showed complete overlap of the identified colonies which confirms these colonies consist of
133 parasites (Fig. 1B). We chose to use Hoechst-staining of DNA as the fluorescent marker as this
134 route enables assessment of clinical isolates without integrated fluorescent markers. At
135 increased magnification (60X and 100X), we show that a colony consists of hundreds-to-
136 thousands of parasites, evidenced by individual parasites and observed hemozoin (Fig. 1C).
137 The growth of parasites results in reduced hemoglobin that appears as an opaque clearing in
138 the red blood cell monolayer, consistent with previous study of plaque forming in *P. falciparum*[15]

139 (Fig. S1A). Z-stacked video of a colony imaged with a 100X objective showed that parasites are
140 distributed horizontally and vertically throughout the packed red blood cell layer (Fig. S1B and
141 Supplementary Video 2).

142 In practice, this can be used to track individual parasites and quantify the growing colony
143 originating from individual parasites (Fig. 1D and S1C). We found long-term measurements at
144 multiple points allow for longitudinal measurements of parasite growth and identification of slow
145 growing or late recovered parasites (Fig. S2). To further validate the single parasite-to-colony
146 concept and quantification reliability, we performed a serial dilution experiment to assess if the
147 number of colonies observed in each well correlates with the estimated number of parasites
148 seeded in each well (Fig. S3A). Measurements of total DNA content showed a successful serial
149 dilution of parasites (Fig. S3B). From the same experiment, quantification of colonies from wells
150 that are seeded with $\leq$2500 cells correlated with the total DNA content of parasites; first two
151 dilution points resulted in too many colonies which lead to inaccurate quantification (Fig. 1E). In
152 columns with lower number of parasites, the average quantified colonies in each column
153 matched up closely to the estimated number of parasites with only one dilution away, likely due
154 to failed replication of some parasites (Fig. 1F). Taken together, these results demonstrate that
155 one colony comes from replication of one single parasite and quantification of colonies can be
156 used to track the original number of viable parasites in each well.

157 **qTRACE tracks single parasite survival, time-dependent recovery and growth**

158 Initially, we developed qTRACE to improve understanding of initial survival and recovery
159 from artemisinin exposure and artemisinin-induced ring stage dormancy phenotypes (Fig. 2A).
160 To ensure sufficient identification of late recovery of dormant parasites, we designed the assay
161 to last 22 days in duration, with multiple timepoints taken throughout (Fig. 2A). One of the most
162 critical aspects of the assay was to prevent liquid movement in the blood layer, since any
163 movement of the static blood layer could disrupt the integrity of colonies. To address this

164 difficulty while being able to perform liquid manipulation throughout the assay, we designed a
165 robotic automation protocol to enable slow media change with essentially no disruption to the
166 blood layer (Figure S4A). At every timepoint, one plate was fixed and stained for HCI while the
167 remaining plates underwent media change using no-disruption protocol (Fig. 2A).

168 We developed single-parasite viability index (SVI) to compute the viability from drug
169 treatment based on quantification of colonies. We introduced a dilution factor (D) between the
170 treated and untreated samples to enable flexible seeding of parasites and normalization of
171 differential growth rate and genotypes of strains. We can determine the viability of single
172 parasites at time t for strain s:

173 $$SVI\ (s,t) = \frac{\text{Treated colony counts (s,t)}}{\text{D(s) x Untreated colony counts (s,t)}} \text{x100}$$

174 SVI is the ratio of the number of colonies between treated and untreated conditions
175 normalized to single parasite division. D(s) is the determined dilution factor between treated
176 sample and untreated sample for strain s. The introduction of factor D enables greater tolerance
177 of experimental variability caused by cell density (Fig. S4B). Additionally, the factor D can be
178 adjusted to compensate for different levels of drug sensitivity of different genotypes. SVI varied
179 slightly under different D factors because the overall percentage of viability remained
180 unchanged (Fig. S4C).

181 Single timepoint qTRACE SVI assessment is usually enough for routine drug killing and
182 parasite surviving evaluation, which requires no media change and can be applied with manual
183 tools (Fig. 2B). In this study, we used day 7 as the first timepoint to assess initial survival from
184 artemisinin exposure. Consecutive measurement of SVI at different timepoint reveals
185 cumulative recovery overtime at single parasite resolution (Fig. 2C). This makes it possible to
186 identify and quantify parasites that recover late. Besides evaluation of multiple parasite strains
187 to a single inhibitor, qTRACE also is compatible with high-throughput drug testing (Fig. 2A). In a

188 dose response experiment, we can assess drug killing effects at different concentrations (Fig.
189 2D). Given SVI for a range of concentrations, SVI50 is the concentration that confers 50%
190 viability.

191 Through quantification of the colony size over time, we can capture the exponential
192 growth of every viable parasite (Fig. 2E). This can be useful to evaluate the drug effects on
193 parasite growth. It is well known that many drugs not only have the cytotoxic effects but also the
194 cytostatic effects on cell growth, yet the measurement of this aspect has not been readily
195 accessible for most standard assays. Moreover, quantification of the area of colonies alongside
196 viability enables identification of late recovered dormant parasites and assess growth behavior
197 of those recovered parasites. To quantitatively determine growth difference between two
198 samples, we adapted the growth rate inhibition metrics (GR) from a previous study[16]:

199 $GR = 2^{k(T)/k(U)}-1$

200 In our application, k(T) is the growth rate of drug-treated parasites and k(U) is the growth
201 rate of untreated controls. The GR value here can be used to assess long-term impact on
202 parasite growth between two conditions. Similarly, the GR value can also be used to
203 quantitatively assess fitness difference between strains, where k(T) became the growth rate of
204 strain 1 and k(U) became the growth rate of strain 2. The GR value ranges from 0 to -1, 1
205 meaning no impact on growth, 0 meaning complete growth inhibition and negative value
206 indicates cytotoxic effects. In a dose response setup, GR is calculated for each concentration
207 and GR50 is the concentration when GR = 0.5. Using GR and SVI together we can differentiate
208 cytotoxic effects and cytostatic effects of a drug.

209 **qTRACE reveals time-dependent viability of single parasites after DHA exposure and**
210 **diverse mechanisms of artemisinin induced dormancy**

211 Mutations in K13 propeller domain are known to facilitate resistance to artemisinin
212 drugs[17]. To study how K13 mutations affect the viability of parasites at individual parasite level,
213 we chose Dd2 and its K13 mutants Dd2-K13-C580Y and Dd2-K13-R539T for comparison with
214 qTRACE[18]. Rings at 0-3hpi were exposed to 700nM DNA for 6 hours followed by plating
215 according to our plate design (Fig. 2A). As expected, we successfully captured the number and
216 the size of growing colonies from all three strains in both treated and untreated conditions, with
217 a much smaller number of colonies from DHA treated Dd2 compared to its K13 mutants (Fig.
218 3A). Overall, both DHA treated and untreated colonies kept growing throughout the assay
219 duration (Fig. S6A). Interestingly, we observed a wide distribution of the size of colonies even in
220 the untreated controls, despite that they were tightly synchronized at the start of the experiment
221 (Fig. S6A). This varying growth rate in the untreated samples is likely genuine biological
222 variability in the growth of *P. falciparum*[19]. qTRACE single timepoint assessment of SVI on day 7
223 revealed the differences in susceptibility to DHA among three strains (Fig. 3B). All three strains
224 continued to show increased viable parasites over time until reaching a plateau, indicating that
225 the initial survivors only represent a fraction of the total parasites that will eventually recover
226 from DHA (Fig. 3C). These results demonstrate that both Dd2 and its K13 mutants utilize
227 dormancy for survival and that K13 facilitated resistance to artemisinin is not only shown in the
228 initial unaffected parasites, but also the number of parasites that can persist via dormancy
229 mechanisms and recover at later time. Dd2-K13-R539T exhibited over 100-fold more viable
230 parasites, while Dd2-K13-C580Y showed a comparatively lower difference compared to the
231 parental Dd2 (Fig. 3D). This is consistent with previous reports showing that the R539T mutation
232 confers a higher level of resistance than C580Y[17, 20]. The fold change remained relatively stable
233 over the course, suggesting that even though the number of parasites recovered were greater
234 for Dd2-K13-C580Y and Dd2-K13-R539T, the overall percentage of late recovered parasites
235 remained similar in all three strains.

236 To investigate if the delayed recovery from DHA is a common strategy of survival, we
237 tested various other laboratory adapted lines and clinical isolates. We tested two parasite lines
238 and their progenies that were previously selected for artemisinin resistance (D6, D6R, W2 and
239 W2R)[8], hoping to gain insights into the difference of artemisinin tolerance between in vitro
240 selected lines and K13 enabled resistance. As expected, W2 and W2R showed different levels
241 of resistance to DHA exposure and continued to have parasites recovered over time (Fig. S5A).
242 The fold change of viability between W2 and W2R decreased with time, meaning W2 have more
243 viable parasites coming from delayed recovery compared to W2R (Fig. S5A). This suggests that
244 the selection of W2R may have enabled parasites to better survive the initial exposure to DHA.
245 In a similar manner as W2 and W2R, D6 and D6R showed increased SVI overtime despite
246 higher susceptibility to DHA (Fig. S5B). The viability difference between D6 and D6R was
247 greater than that between W2 and W2R, presumably because D6R went through a longer
248 selection period than W2R[8] (Fig. S5B). Overall, these in vitro selected parasites exhibited
249 weaker resistance compared to K13 enabled resistance, yet recovery from artemisinin-induced
250 dormancy was observed in both genotypes (Fig. 3C, S5A and S5B). We next tested NHP-4781
251 which has E252Q K13 mutation outside propeller domain[21]. NHP-4781 showed a comparative
252 level of susceptibility to DHA exposure compared to Dd2, indicating that mutation outside
253 propeller domain on K13 does not incur resistance to artemisinin, which is consistent with
254 previous findings[20] (Fig. 3E and Fig. S5C). C235 is a multi-drug-resistant parasite derived from
255 patient with treatment failure[22]; it showed elevated resistance compared to D6 and Dd2, but not
256 W2 (Fig. 3E and Fig. S5C). The ability to have more continuous dormancy recovery of W2
257 compared to other parasite strains is consistent with previous study which showed higher and
258 longer recovery from W2[14] (Fig. 3E).

259 Across the nine parasite strains tested, they showed different levels of delayed recovery
260 from DHA (Fig. S5D). Notably, the initial survival measured on day 7 from DHA strongly

261 correlates with late recovery, indicating that, despite the differences of susceptibility to DHA
262 among these parasites, the survival is equally exhibited by the initially survived parasites and
263 parasites recovered from dormancy (Fig. 3F). For many of the artemisinin sensitive parasite
264 lines, delayed recovered dormant parasites accounted for about half of the total parasites that
265 eventually survived DHA exposure (Fig. 3G). Decreased proportion of late recovered parasites
266 in both K13 mutants and in vitro selected lines suggest that increased level of resistance
267 reduced the reliance on dormancy as a mechanism to survive (Fig. 3G). The large portion of
268 delayed recovered parasites is often overlooked in many studies but now can be more
269 accessibly evaluated using qTRACE.

270 **qTRACE assesses growth inhibition and fitness**

271 Through measurements of the growing colonies, qTRACE allowed us to quantify growth
272 inhibition imposed by drugs as well as the fitness differences between parasite lines. From the
273 same DHA exposure experiments described above, we analyzed the growth and distribution of
274 colonies of DHA treated Dd2, Dd2-K13-C580Y and Dd2-K13-R539T. We found the growth of the
275 two K13 mutants mimic their untreated control, while the growth of Dd2 was severely affected
276 by DHA, as evidenced by the dispersed distribution (Fig. 4A). The growth curve of DHA treated
277 Dd2 showed a reduced growth rate compared to its control, whereas the growth curve of the
278 DHA treated K13 mutants overlaps with that of their controls (Fig. 4B). This is also manifested
279 by the lower GR value in the Dd2 compared to its Dd2 K13 mutants (Fig. 4C). These results
280 suggest that Dd2 K13 mutant parasites can quickly adapt to normal growth once recovered from
281 DHA, but the growth of many parental Dd2 parasites become impaired by DHA. Many previous
282 studies showed that adaptation to drug resistance sometimes induces fitness costs in the
283 parasites[9, 23]. Through qTRACE, we identified the fitness disadvantage in the Dd2-K13-C580Y,
284 but not in the Dd2-K13-R539T, compared to parental Dd2; which is consistent with previous
285 reports[20] (Fig. 4D). In the case of in vitro selected lines, W2R showed a fitness disadvantage

286 compared to W2, while D6R showed a more minor disadvantage compared to D6 (Fig. S6B).
287 DHA exposure resulted in reduced growth and lowered GR for W2, yet W2R phenocopied the
288 growth of untreated conditions (Fig. S6C). Similarly, D6 showed growth delay when exposed to
289 DHA, while D6R was not affected (Fig. S6D). C235 showed a slight impact on growth rate from
290 DHA exposure (Fig. S6E). NHP-4781 also exhibited retarded growth following DHA exposure,
291 as well as poor adaptation to culture as seen by the slow growth (Fig. S6F). This is supported
292 by the observed gametocyte formation even during routine culture. Total viability from
293 artemisinin exposure showed a moderate correlation with GR, indicating that increased
294 resistance to artemisinin lead to decreasing growth impact on the viable parasites, but is also
295 parasite background dependent (Fig. 4E). Together, these results demonstrate that resistance to
296 artemisinin is also reflected in the ability to quickly resume growth upon recovery.

297 **Application of qTRACE in drug testing**

298 The ability to assess phenotypes of single parasites is a valuable tool to improve
299 accuracy of drug susceptibility testing (Fig. 2A). We applied qTRACE in a typical drug screening
300 and tested 15 common anti-malarial drugs on Dd2 parasite (Fig. S7A and Supplementary Table
301 3). Consistent with previous reports of Dd2 background, qTRACE also identified the elevated
302 resistance to sulfadoxine and pyrimethamine in Dd2[24]. SVI50 of most of the compounds tested
303 showed comparable results to the standard IC50 measurements in a bulk culture, indicating
304 strong reproducibility of qTRACE to serve as a quantitative alternative to conventional bulk
305 methods (Fig. S7B and Supplementary Table 3). qTRACE also demonstrated extraordinary
306 efficiency and improvements of throughput due to very low parasite input requirements (less
307 than 50 parasites per well).

308 **qTRACE AI powered by deep learning enables continuous label-free live cell analysis**

309 From the development of qTRACE, we realized one of the major limitations is the lack of
310 continuity between every timepoints in a continuous experiment. For an experiment of 6
311 timepoints, 6 independent plates are required, each of the plates end at one timepoint (Fig. 2A).
312 This leads to wasted resources, lost insights and inaccurate quantification of single parasite
313 growth since there is inherent variability between each plate.

314 To overcome limitations, we incorporated a deep learning-based semantic segmentation
315 method into the original qTRACE. The next generation qTRACE AI directly quantifies objects on
316 images acquired through transmitted light microscopy without the need to stain or fix. A total of
317 5760 distribution calibrated images covering diverse experimental applications were used to
318 train convolutional neural networks (CNN) (Fig. 5A). These images covered a wide range of
319 time points to include both early small colonies and later large colonies, but with a stronger
320 focus on early times to compensate for increased difficulty of learning of small colonies (Fig. 5B
321 and S8A). Parasite colonies of every transmitted light image were annotated to polygons by
322 trained human professionals using ground truth GFP images as reference (Fig. 5C). We chose
323 512×512 pixels as the training standard due to its balance between preserving sufficient spatial
324 morphological information and reducing computational overhead.

325 We trained on CNN model U-Net architecture because of its established capability of
326 biomedical level semantic segmentation (Fig. 5D and S8B). Overall, qTRACE AI achieved
327 comparable human level accuracy, demonstrated by the strong correlation between annotated
328 results and model predicted results (Fig. 5E). Mean absolute error (MAE) of count quantification
329 showed an average of 2.63 and is relatively stable over time, while area pixel error increased
330 slightly in later timepoints (Fig. 5F and Supplementary Table 4). Most of the test images showed
331 identical quantification between annotated results and predicted results across various
332 conditions (Fig. S9A). However, the true accuracy of qTRACE AI is underestimated here
333 because we noticed most of the disparities between annotated results and predicted results

334 were due to human errors in annotations. In almost all instances, our trained CNN model was
335 able to correct human errors, including filtering debris and false positives, and identify true
336 colonies that were originally omitted by mistakes (Fig. S9B and S9C). Besides, the label-free
337 image analysis of qTRACE AI removed the most common challenge of dealing with noise during
338 fluorescent imaging as we routinely saw images that would have been unsuitable for analysis if
339 used fluorescent imaging alone (Fig. S9D). Since qTRACE AI uses a novel quantification
340 method to measure single parasite growth and there is no benchmarking available, we decided
341 to train a second model using Vision Transformers (ViT) to allow for performance comparison
342 (Supplementary Table 4). Overall, U-Net architecture showed superior performance compared
343 to ViT for both count and area quantification tasks (Supplementary Table 4). The performance
344 differences between architectures may be attributed to the data-efficiency characteristics of
345 each model. Thus far, the capability of qTRACE AI to track live single parasite greatly enhanced
346 accuracy, flexibility and allowed authentic time-lapse cellular information linkage over original
347 protocol, making it more suitable for diverse applications, including demanding long-term
348 studies (Fig. 5G).

349 **qTRACE reveals new insights into drug activities and effects**

350 To assess qTRACE AI, we screened the Medicines for Malaria Venture (MMV)
351 antimalarial reference library and compared the results to original qTRACE. The compounds in
352 the library were serially diluted and tested to derive both SVI50 and GR50 using qTRACE AI
353 label-free imaging analysis (Fig. 6A). Correlation study of qTRACE AI and qTRACE side by side
354 showed excellent reproducibility between the two for viability and growth assessments (Fig. 6B).
355 Most of the tested drugs showed similar dose response curve between qTRACE AI and
356 qTRACE (Fig. S10A). These results confirmed the feasibility of qTRACE AI to obtain validated
357 results from real experimental applications. Through the evaluation of SVI50 and GR50, we
358 identified diverse drug induced cytotoxic and cytostatic effects from tested compounds. (Fig. 6C

359 and Supplementary Data 1). Azithromycin showed strong growth inhibition evidenced by the
360 much lower GR50 and the inhibition of growth at lower concentration as seen in the GR curve,
361 while pantothenamide showed clear cytotoxic preferred effect (Fig. 6C and S10B).
362 Understanding time-dependent drug effects is crucial for dosing and pharmacokinetic studies.
363 To take advantage of the unlimited continuous live cell imaging of qTRACE AI, we performed a
364 time-lapse experiment testing the time-dependent potency of compounds from the same cells
365 over time. We observed all three types of time-dependent activities, either increasing,
366 decreasing or stable over time (Fig. 6D). We detected 23 drugs gradually lost potency, while
367 only 3 drugs gained extra potency with at least 2-fold change over time (Fig. 6D and
368 Supplementary Data 1). Azithromycin showed the greatest potency increase in the library, and
369 mirincamycin is another known slow acting drug (Fig. 6E). KAE609, KAF156 and some other
370 drugs showed strong stability over time, while many of the drugs lose their effect over time (Fig.
371 6E and Supplementary Data 1). From these results, we conclude that qTRACE is capable of
372 being used as a superior replacement for conventional drug testing to reveal more insightful
373 drug effects from single parasite resolution.

374

375

376

377

378

379

380

381

382 **Discussion**

383 In this study we demonstrated that qTRACE is a versatile single parasite quantitative
384 method for evaluation of parasite viability and drug induced effects. qTRACE overcame many of
385 the limitations in existing methods to provide more insightful and comprehensive assessments
386 of drug-parasite interactions. We show here that qTRACE can be applied to assess differences
387 between parasite strains to a drug of interest or drug effects in a high throughput screen. The
388 ability of qTRACE to quantify the viability and growth simultaneously on a single parasite basis
389 ensured accurate and unbiased differentiation of individual level diversity in long-term
390 experiments. Using artemisinin as an example drug, we showed how artemisinin induced
391 dormancy contributes to overall recrudescence. Application of qTRACE in drug testing
392 demonstrated superior efficiency and new discoveries of drug induced phenotypes. Integration
393 with deep learning-based analysis, qTRACE AI demonstrated unparallelled enhancements of
394 generalization, accuracy and biological authenticity over original protocol.

395 The development of qTRACE was originally driven by the mission to elucidate the
396 confounders in artemisinin induced dormancy and infection recrudescence. Numerous studies
397 have suggested the association between artemisinin resistance and artemisinin induced
398 dormancy, yet there is a lack of answers due to limitations on current approaches[8, 9, 11, 14, 25].
399 qTRACE solves those limitations by tracking the viability and growth of individual parasites,
400 thereby effectively distinguishing initial survivors and late recovered parasites in an automated
401 high throughput manner. Our results confirmed that recovery from artemisinin-induced
402 dormancy plays a huge role in overall parasite survival at the population level, with nearly half of
403 the viable parasites arising from dormancy recovery. Given that day 7 was the first point of
404 measurement, the proportion of delayed recovery is likely underestimated. So far, K13 mutation
405 in the propeller domain is the only known marker of clinically relevant artemisinin resistance[17]. In
406 this study, we show that the ability to survive artemisinin drugs in K13 mutants are not only

407 exhibited by the large number of initial survivals, but also in the delayed recovery from
408 dormancy (Fig. 3C, 3F and 3G). In fact, the number of parasites recovered from dormancy could
409 be underrated due to limited space in the well for higher resistant lines (both Dd2 K13 mutants)
410 in later timepoints (Fig. 3C). The ability to utilize dormancy as a survival mechanism in both
411 sensitive and resistant parasites suggest dormancy is an innate survival mechanism and likely
412 independent of genomic resistance mechanisms. When selected for artemisinin resistance,
413 naturally or in vitro, initial survivors and late covered ones are both being selected because the
414 selection process is continuous, as supported by the strong correlation between initial survival
415 and dormancy recovery (Fig. 3F). The ability to use dormancy as a survival mechanism is
416 determined by the initial response to artemisinin. Resistance mechanisms improve initial
417 adaptation and stress response to artemisinin drugs through each of their pathways, allowing
418 more parasites to survive as well as more parasites to utilize dormancy. On the other hand,
419 more sensitive parasites have overall lower initial survival and lower dormancy usage due to
420 poor initial response to artemisinin. Previous study suggests that dormant parasites are resilient
421 to a wide spectrum of anti-malarial drugs, indicating the reduced efficacy of ACT partner drugs
422 to remove dormant parasites[11]. Given the large portion of late recovery after DHA exposure, it
423 would be reasonable to attribute the clinically observed recrudescence to the recovery of
424 dormant parasites. In fact, parasites going into dormancy may be a favored survival path during
425 ACT treatment because of the reduced susceptibility to drugs and the half-lives of the partner
426 drug.

427 Investigation of cytostatic drug effects and fitness costs associated with increased
428 resistance constitute a large study domain in drug discovery and drug resistance. The cytostatic
429 effects of many anti-malarial drugs remain poorly studied due to lack of approaches to properly
430 evaluate them in a large scale. The ability to track individual parasites with qTRACE made it
431 possible to evaluate cytostatic effects in a high throughput and technically straightforward

manner. For the first time, we show that growth inhibition is another drug effect after DHA exposure. Across nine parasite lines, we observed varying cytostatic effects induced by artemisinin, influenced by genetic backgrounds and a moderate correlation of declined growth inhibition to increased resistance.

Altogether, our results demonstrate that resistance to artemisinin is a multifarious phenotype. When resistance increases, the proportion of initial survival and recovery from dormancy equally increases, the impact on growth gradually decreases until there is no more growth impact but in a parasite background dependent way. The dormancy effects of artemisinin drugs cannot be underestimated and maybe the ultimate culprit behind frequently reported recrudescence. It is imperative that future ACT development and artemisinin resistance studies incorporate dormancy recovery as a standard evaluation.

Previous studies on fitness typically include laborious processes and error prone techniques, such as large amount of microscopy counting or combining two different parasites into one culture[9, 23, 26]. In this study, we showed that fitness assessment is a convenient secondary outcome when conducting qTRACE for other purposes, such as testing inhibitor effect. With the emergence of qTRACE, fitness study will no longer need to be a complicated independent experiment. The growth assessment capability of qTRACE will be useful to a wide range of research, including but not limited to evaluating growth competition and growth inhibition, such as one imposed by RNAi or nutrition starvation.

Integration of deep learning-based analysis into qTRACE AI effectively overcame the limitation of having disconnected results at every timepoint. U-Net architecture CNN model is well suited for qTRACE, evidenced by strong learning of the pattern with limited datasets. We found that qTRACE AI is superior to original qTRACE for its excellent generalization, accuracy and cellular information linkage. qTRACE AI uses a single pipeline for all the experimental conditions, while in many cases different sets of rules are needed for original qTRACE

457 depending on the timepoints or applications. qTRACE AI provides unparalleled flexibility for
458 complex experiments allowing one to perform unlimited handling and observations. Debris and
459 background signals are among the most difficult noises to remove in rule-based image analysis
460 because most of the time they fall into similar characteristic regions to the true objects. False
461 positives in a supposedly empty image tend to cause the most devastating bias. qTRACE AI
462 demonstrated extraordinary ability to handle those difficult situations (Fig. S9B, S9C and S9D).
463 Lastly, label-free continuous live cell observation ensured the most authentic connection of cell
464 behavior over time, significantly improved the ability to identify unique signatures for each
465 individual parasite. qTRACE AI and original qTRACE will serve as great complement for each
466 other to improve versatility and accessibility.

467 Drug screening application of qTRACE demonstrated its ability to serve as a direct
468 replacement to currently used dose response assays. SVI50 and GR50 derived from qTRACE
469 are robust alternatives to IC50 as the measurements were derived from per parasite basis. For
470 routine drug testing, a single endpoint at 120h is sufficient to identify different effects and does
471 not require any robotic automation. Taking advantage of deep-learning powered continuous
472 label-free imaging, we screened the anti-malarial reference library and revealed new insights
473 into both cytotoxic and cytostatic effects imposed by a drug, which will improve understanding of
474 the mode of action of a drug and future development. Through continuous measurements,
475 qTRACE outputs time-dependent drug potency shift, which can serve as foundation for drug
476 pharmacokinetics and drug combination study. Equally important to accurate effect evaluation is
477 the improved efficiency, qTRACE increases drug screening throughput by up to 667%. Typical
478 dose response assay uses >1% parasitemia culture (~2000 parasites/μl in 2% hematocrit),
479 while qTRACE only needs less than 3 parasites/μl.

480 qTRACE is based on the biological phenomenon that a single parasite grows into a
481 colony. The concept of colonies and plaque assays have been widely used in various biological

research. In malaria research, similar concepts have been previously proposed, yet there has been little application and require visual inspection of plaques[15]. The formation of colony in a *P. falciparum* culture is inherently difficult because the cultures are typically in a larger volume of liquid and parasites tend to swim to other areas, not to mention the lack of accurate quantification methods. Integrated with HCI, automation and deep learning, we show a versatile application of this biological phenomenon, meanwhile removing many of the previously suggested limitations, such as long waiting time and hematocrit limits. The flexibility to change media and supplement fresh blood is crucial for any long duration experiments. Here we have demonstrated that currently available compact automation stations are sufficient to achieve media change without disrupting colony integration, though it's not required for many of the applications shown in the paper. Potential applications of this concept are far beyond what has been demonstrated in this study. Because of the ability to identify the number of colonies in each well, it becomes possible to map genomic and transcriptomic signatures associated with differential conditions at monoclonal levels. More advanced utilization could improve the selection of drug resistance by picking parasites that recover early or recover late, depending on if the purpose was to select for initial survivors or study latency mechanism.

In summary, qTRACE will serve as an all-around method that can be used for a wide range of scenarios, effectively overcoming previous limitations to achieve single parasite level insights. It would be appropriate to use qTRACE as a routine assessment of the recrudescence risks of developing compounds and current treatment combinations.

506 **Methods**

507 **Parasite culture**

508 The parasites used in this study include Dd2, Dd2-K13-C580Y and Dd2-K13-R539T (genetically
509 modified Dd2 strains containing mutation on K13 PF3D7_1343700); D6 and D6R (an in vitro
510 selected artemisinin resistant progeny of D6); W2 and W2R (an in vitro selected artemisinin
511 resistant progeny of W2); C235; NHP-4781; and a genetically modified NF54-GFP (inserted
512 GFP in cg6 locus)[8, 18, 22, 27]. For routine culture, parasites were grown at 37°C at 2% hematocrit
513 in RPMI 1640 media (Gibco) supplemented with 25mM HEPES and 24mM $NaHCO_3$, and with
514 10% heat-inactivated human A+ plasma and 10 µg/ml gentamycin. Cultures were maintained in
515 a gas chamber with 5% O_2, 5% CO_2, and 90% N_2. Giemsa slides were routinely made to assess
516 parasite growth and stages. The growth media was changed every two days, and fresh blood
517 was added when needed. Cultures were tested and found negative for mycoplasma regularly
518 during this study.

519 **Ring Stage 0-3hpi Synchronization**

520 The same 2-step synchronization protocol was performed to achieve 0-3h post invasion (hpi) for
521 all strains used in this study. First, late stages were selected by laying on top of 65% percoll
522 gradient and followed by centrifugation at 1500RCF[28]. Three hours later, freshly invaded rings
523 were selected using 5% D-sorbitol [29]. After each synchronization step, parasites were washed
524 with RPMI 1640 media. Synchronized 0-3hpi parasites were allowed to reinvade before being
525 used for experiments.

526 **Dihydroartemisinin (DHA) exposure**

527 The same DHA treatment was used for all DHA exposure experiments in this study. Tightly
528 synchronized 0-3hpi parasites were adjusted to 1% parasitemia and 2% hematocrit and treated

529 with 700nM DHA. Six hours later, DHA was removed by centrifugation and washing with RPMI
530 1640 media before being replaced with culture media.

531 **GFP live cell time lapse imaging and fluorescent imaging**

532 For GFP continuous imaging, 0-3hpi NF54-GFP parasites were seeded into 384 well plates
533 (Greiner Bio-one) with an estimated number of 10 parasites per well. The same plate was taken
534 for imaging on day 3, 5, 7, 10, 13, 16, 19, 22 using Lionheart (Agilent). Media was changed at
535 day 7, 10, 13, 16, 19 by removing and replacing 20µl of media using NXP workstation
536 (Beckman). Another experiment with 6h DHA exposure was performed in a similar way except
537 the initial plated parasites were 1000 parasites per well. To image parasite using both Hoechst
538 staining of DNA and GFP expression, 40ul of 5ug/ml Hoechst was added into the plate and
539 maintained for 30 minutes before imaging. High magnification images were obtained using the
540 100x objective on a DeltaVision II (GE Healthcare) with deconvolution of a 22-plane Z-stack
541 using Software (GE healthcare).

542 **qTRACE**

543 **Metrics**

544 Colony counts and colony areas in the presence of drug are normalized to untreated controls in
545 the same plate under the same growth conditions. Technical replicates were averaged to yield
546 an average colony counts or colony area. For single candidate testing, we typically collect from
547 48-176 technical replicates. For dose response, two technical replicates per plate were
548 collected.

549 Single-parasite viability index (SVI) was calculated to evaluate the viability of parasites and the
550 cytotoxic effects of the testing drugs. SVI of parasite strain (s) at timepoint (t) was calculated as:

551 $$SVI\ (s,t) = \frac{\text{Treated colony counts (s,t)}}{\text{D(s)x Untreated colony counts (s,t)}} \text{ x } 100$$

552 The average number of colonies for each parasite strain growing at each condition at every
553 timepoint was calculated and normalized to the average number of colonies from the control.
554 (D) represents the dilution factor between treated and untreated in a multi-strain testing design.
555 SVI is a percentage value and ranges from 0 to 100, 0 meaning no viable parasite exists and
556 100 means no effect on parasite viability from the treatment condition. In recovery experiments,
557 Survival SVI is defined as the SVI form the first point of measurement. The Max SVI
558 measurement after the first timepoint is defined as the maximum possible viability or max SVI.
559 Maximum delayed recovery is calculated as Max SVI – Survival SVI. When calculating SVI for a
560 range of concentrations, SVI50 is the concentration that confers half maximal drug effect on
561 parasite viability.

562 Growth rate inhibition (GR) was adapted from a previous study to evaluate the growth of every
563 viable parasite[16]. The average area of colonies for each parasite strain growing at each
564 condition at every timepoint was calculated and normalized to the average area of colonies from
565 control. GR value ranges from -1 to 1, with 1 meaning no impact on growth, 0 meaning
566 complete growth inhibition, and -1 meaning highest cytotoxicity. When calculating GR for a
567 range of concentrations, GR50 is the concentration when GR = 0.5, which refers to half maximal
568 growth inhibition.

569 For continuous measurements from multiple timepoints, an exponential growth curve was fitted
570 for each parasite strain and each condition. GR was then calculated:

571 $GR = 2^{k(T)/k(U)}-1$

572 The growth rate (k) of each fitted curve was extracted, with k(T) representing the growth rate of
573 drug treated condition and k(U) representing the growth rate of untreated controls. Alternatively,
574 when testing fitness or growth competition between two strains, k(T) became the growth rate of
575 strain 1 and k(U) became the growth rate of strain 2 or reference strain.

576 When measuring qTRACE as a single timepoint experiment, GR was calculated as:

577 $$GR = 2^{\frac{log_2(x(T)/x_0)}{log_2(x(U)/x_0)}} - 1$$

578 In this equation, x(T) represents the average area in drug treated conditions and x(U) is the
579 average area in untreated control. X_0 is the starting area; this could be the measurement before
580 starting the experiment or be fitted as an estimated area of a single parasite because colonies
581 originate from single replicating parasites.

582 **Single candidate qTRACE**

583 This method was designed to test the response of multiple parasite lines to a single testing
584 candidate of interest. In this study, DHA was used as an example. Synchronized 0-3hpi
585 parasites were treated with DHA for 6h using the procedure described above. An estimated
586 number of 10-50 parasites per well were seeded for untreated control for each parasite line.
587 Depending on the designed D factor for each parasite line, D*number of parasites in untreated
588 controls for each treated samples were seeded into the same plates with the untreated controls
589 based on similar design shown in Fig. 2A. Based on different timeline design, at every timepoint,
590 one plate was taken for staining and thereafter imaging quantification; the rest of the plates
591 were taken for media change using designed no disruption protocol on NXP workstation to
592 minimize blood layer disruption.

593 **Evaluating altering condition of qTRACE**

594 Altering condition experiments were performed to characterize the tolerance of qTRACE to
595 variations. For changing seeding density, D = 100 was used and the estimated seeding parasite
596 in untreated wells ranged from 5-50. For changing D factor, an estimated 30 parasites per well
597 in untreated wells were used.

598 **Dose response qTRACE**

599 This method was designed to test the effect of compounds in a high throughput format using
600 qTRACE. Compounds were tested in a 12-point semi log dilution in duplicates. Synchronized 0-
601 3hpi parasites were seeded into 384 well plates with 50-100 parasites per well. The seeded
602 plates were then drugged with the source plate using pintool affixed to the NXP (V&P Scientific).
603 For single endpoint experiments, plates were fixed and stained at 120h. For time lapse
604 experiments, whole plates were imaged using transmitted light at 48h interval followed by
605 qTRACE AI analysis.

606 **Curve fitting**

607 For experiments containing multiple timepoint, an exponential growth curve was fitted using the
608 average colony area measured at each timepoint for each condition:

609 $Y = Y_0 * \exp\,(K * t)$

610 The fitted parameters are:

611 Y_0: the best fitted starting value when t = 0.

612 K: the growth constant of the fitted curve for the condition and parasite line used

613 t: time

614 In the case of a comparison between two fitted curves, Y_0 was restricted to untreated control or
615 the reference parasite strain. K was extracted for calculation of GR.

616 In dose response experiments, SVI and GR of each concentration at each timepoint for each
617 drug is calculated, then fitted into a sigmoidal curve:

618 $\mathrm{SVI}\,(\mathrm{c}) = \mathrm{SVI}_{\mathrm{min}} + \frac{100-SVI_{min}}{100+(\frac{c}{SVI50})^{hSVI}}$ $\mathrm{GR}\,(\mathrm{c}) = \mathrm{GR}_{\mathrm{min}} + \frac{1-GR_{min}}{1+(\frac{c}{GRE50})^{hGR}}$

619 The fitted parameters are:

620 SVI_{min} or GR_{min}: the maximum possible effect of a drug on parasite viability or growth inhibition
621 in a fitted curve

622 hSVI or hGR: the hill slope coefficient of the fitted curve

623 SVI50 or GRE50: the concentration that confers half maximal effect on parasite viability or half
624 maximal effect in GR curve.

625 **Imaging and quantification, and transmitted light imaging for deep learning**

626 For fixed timepoints, plates were fixed and stained with 5µg/ml Hoechst and 1% glutaraldehyde.
627 Imaging was performed using Lionheart FX (Biotek) or ImageXpress (Molecular device). Whole
628 wells were captured for all 384 wells with 4X magnification. DAPI intensity and focus was
629 determined using untreated wells as reference High content analysis was performed using
630 image metrics including colony number, size, area, and signal intensity. We found a minimum
631 size of 20 µm of colonies to allows for most optimal removal of small backgrounds and small
632 artefacts. The number of colonies and the area of each colony were then exported for further
633 analysis. Identified outliers were verified on the corresponding images and then discarded.

634 NF54-GFP parasite was used for the generation of deep learning training datasets. Whole well
635 transmitted light images were acquired with 4X magnification using ImageXpress. The same
636 sample was first imaged through transmitted light microcopy then immediately followed by GFP
637 channel to acquire GFP reference image. In a continuous experiment, the plate was returned to
638 culture condition and imaged again at next timepoint.

639 **Image processing and training data preparation**

640 Original TIFF image with resolution of 2048×2048 and depth of 16-bit grayscale was first
641 normalized to 2048×2048 resolution and 8-bit RGB format. The edge of every image was
642 cropped by 150 pixel to remove areas with uneven illumination. All polygon annotations were

643 initially performed by human professionals. Quality checks of all images and masks were
644 performed with at least two rounds of random selections by two independent reviewers. To
645 optimize computational efficiency and maintain consistent input dimensions across the dataset,
646 all images were downsampled to 512×512 pixels using the Lanczos resampling algorithm[30]. To
647 enable rapid data loading during the iterative training process, all standardized images and their
648 corresponding segmentation masks were subsequently converted to NumPy array format. The
649 dataset was randomly partitioned into training (70%), validation (15%), and test (15%) sets.

650 **Deep learning CNN U-Net model training**

651 For semantic segmentation, we implemented a U-Net architecture comprising an encoder–
652 decoder structure[31]. The encoder comprises four downsampling stages with 2×2 max pooling,
653 progressively increasing the number of feature channels from 64 to 128, 256, and finally 512.
654 Each stage uses two 3×3 convolutional layers with batch normalization and ReLU activation to
655 capture contextual and morphological features[32]. At the bottleneck, feature maps are processed
656 by a double convolution block with 1024 channels to capture high-level semantic features. The
657 decoder mirrors the encoder with four upsampling stages using 2×2 transposed convolutions.
658 Skip connections concatenate encoder features with decoder outputs to preserve spatial details,
659 followed by double convolution blocks for refinement. A final 1×1 convolution produces the
660 single-channel segmentation map for binary classification.

661 The model was trained using the Adam optimizer with an initial learning rate of 1×10^{-4} and an
662 adaptive scheduler that reduced the rate after 5 stagnant validation epochs[33]. Training was
663 conducted over 50 epoch with a batch size of 32, and validation performance was monitored to
664 prevent overfitting. The final model was selected based on the best validation score, with all
665 metrics reported on a held-out test set.

666 **Colony quantification**

Following segmentation, automated quantification of colony number and area was performed on the predicted binary masks, where white regions (pixel value = 1) represent identified colonies and black regions (pixel value = 0) represent background. Colony enumeration was achieved through connected component labeling. We employed 8-connectivity (Moore neighborhood) for the connected component analysis, which considers pixels connected through both edges and corners as belonging to the same colony. The algorithm iteratively groups adjacent positive pixels until all connected regions are identified, with the total number of distinct labels corresponding to the colony count. Colony areas were quantified by calculating the sum of positive pixels within each segmented region. The total colonization density for each image was computed as the aggregate sum of all positive pixels in the binary mask.

Performance evaluation and metrics

To evaluate colony enumeration, we used Mean Absolute Error (MAE), Root Mean Squared Error (RMSE), Exact Match Rate, tolerance-based accuracy (±1 and ±2 colonies), and the Pearson correlation coefficient to assess counting precision and consistency.

For colony segmentation, we evaluated performance using standard pixel-wise metrics, including Intersection over Union (IoU), pixel accuracy, precision, recall, and F1 score, computed from binary masks of predicted and ground truth annotations.

Vision transformer for semantic segmentation

As an alternative approach to the U-Net architecture, we implemented a Vision Transformer (ViT) model adapted for semantic segmentation. All 512×512 input images were divided into non-overlapping patches of 16×16 pixels, resulting in a sequence of 1024 patches (32×32 grid). To preserve spatial information, learnable position embeddings are added to the patch embeddings, which were then processed through a stack of transformer encoder layers, with layer normalization and residual connections.

For adapting the transformer to dense prediction, the sequence of output embeddings from the final transformer layer must be reshaped back to a 2D spatial representation and upsampled to match the original image resolution. This is achieved through a decoder head that first reshapes the patch tokens back to their spatial configuration, then applies successive upsampling layers to recover the full 512×512 resolution, ultimately producing pixel-wise binary predictions for colony segmentation. We followed the same training strategy and image processing settings for ViT model as well.

1. Witkowski B, Amaratunga C, Khim N, Sreng S, Chim P, Kim S, Lim P, Mao S, Sopha C, Sam B, Anderson JM, Duong S, Chuor CM, Taylor WR, Suon S, Mercereau-Puijalon O, Fairhurst RM, Menard D. Novel phenotypic assays for the detection of artemisinin-resistant Plasmodium falciparum malaria in Cambodia: in-vitro and ex-vivo drug-response studies. Lancet Infect Dis. 2013;13(12):1043-9. Epub 20130911. doi: 10.1016/s1473-3099(13)70252-4. PubMed PMID: 24035558; PMCID: PMC5015432.
2. Davis SZ, Singh PP, Vendrely KM, Shoue DA, Checkley LA, McDew-White M, Button-Simons KA, Cassady Z, Sievert MAC, Foster GJ, Nosten FH, Anderson TJC, Ferdig MT. The extended recovery ring-stage survival assay provides a superior association with patient clearance half-life and increases throughput. Malaria Journal. 2020;19(1):54. doi: 10.1186/s12936-020-3139-6.
3. Baniecki ML, Wirth DF, Clardy J. High-Throughput Plasmodium falciparum Growth Assay for Malaria Drug Discovery. Antimicrobial Agents and Chemotherapy. 2007;51(2):716-23. doi: doi:10.1128/aac.01144-06.
4. Quashie NB, Duah NO, Abuaku B, Quaye L, Ayanful-Torgby R, Akwoviah GA, Kweku M, Johnson JD, Lucchi NW, Udhayakumar V, Duplessis C, Kronmann KC, Koram KA. A SYBR Green 1-based in vitro test of susceptibility of Ghanaian Plasmodium falciparum clinical isolates to a panel of anti-malarial drugs. Malaria Journal. 2013;12(1):450. doi: 10.1186/1475-2875-12-450.
5. Amaratunga C, Neal AT, Fairhurst RM. Flow cytometry-based analysis of artemisinin-resistant Plasmodium falciparum in the ring-stage survival assay. Antimicrob Agents Chemother. 2014;58(8):4938-40. Epub 20140527. doi: 10.1128/aac.02902-14. PubMed PMID: 24867976; PMCID: PMC4136004.
6. Pandit K, Surolia N, Bhattacharjee S, Karmodiya K. The many paths to artemisinin resistance in Plasmodium falciparum. Trends Parasitol. 2023;39(12):1060-73. Epub 20231011. doi: 10.1016/j.pt.2023.09.011. PubMed PMID: 37833166.
7. Codd A, Teuscher F, Kyle DE, Cheng Q, Gatton ML. Artemisinin-induced parasite dormancy: a plausible mechanism for treatment failure. Malaria Journal. 2011;10(1):56. doi: 10.1186/1475-2875-10-56.
8. Tucker MS, Mutka T, Sparks K, Patel J, Kyle DE. Phenotypic and genotypic analysis of in vitro-selected artemisinin-resistant progeny of Plasmodium falciparum. Antimicrob Agents Chemother. 2012;56(1):302-14. Epub 20111114. doi: 10.1128/aac.05540-11. PubMed PMID: 22083467; PMCID: PMC3256069.
9. Hott A, Tucker MS, Casandra D, Sparks K, Kyle DE. Fitness of artemisinin-resistant Plasmodium falciparum in vitro. J Antimicrob Chemother. 2015;70(10):2787-96. Epub 20150722. doi: 10.1093/jac/dkv199. PubMed PMID: 26203183; PMCID: PMC4668880.
10. Witkowski B, Lelièvre J, Barragán MJ, Laurent V, Su XZ, Berry A, Benoit-Vical F. Increased tolerance to artemisinin in Plasmodium falciparum is mediated by a quiescence mechanism. Antimicrob Agents Chemother. 2010;54(5):1872-7. Epub 20100216. doi: 10.1128/aac.01636-09. PubMed PMID: 20160056; PMCID: PMC2863624.
11. Tripathi J, Stoklasa M, Nayak S, En Low K, Qian Hui Lee E, Duong Tien QH, Rénia L, Malleret B, Bozdech Z. The artemisinin-induced dormant stages of Plasmodium falciparum exhibit hallmarks of cellular quiescence/senescence and drug resilience. Nature Communications. 2024;15(1):7485. doi: 10.1038/s41467-024-51846-0.

12. White NJ, Watson J, Ashley EA. Split dosing of artemisinins does not improve antimalarial therapeutic efficacy. Sci Rep. 2017;7(1):12132. Epub 20170921. doi: 10.1038/s41598-017-12483-4. PubMed PMID: 28935919; PMCID: PMC5608907.
13. Barrett MP, Kyle DE, Sibley LD, Radke JB, Tarleton RL. Protozoan persister-like cells and drug treatment failure. Nature Reviews Microbiology. 2019;17(10):607-20. doi: 10.1038/s41579-019-0238-x.
14. Teuscher F, Gatton ML, Chen N, Peters J, Kyle DE, Cheng Q. Artemisinin-induced dormancy in plasmodium falciparum: duration, recovery rates, and implications in treatment failure. J Infect Dis. 2010;202(9):1362-8. doi: 10.1086/656476. PubMed PMID: 20863228; PMCID: PMC2949454.
15. Thomas JA, Collins CR, Das S, Hackett F, Graindorge A, Bell D, Deu E, Blackman MJ. Development and Application of a Simple Plaque Assay for the Human Malaria Parasite Plasmodium falciparum. PLoS One. 2016;11(6):e0157873. Epub 20160622. doi: 10.1371/journal.pone.0157873. PubMed PMID: 27332706; PMCID: PMC4917082.
16. Hafner M, Niepel M, Chung M, Sorger PK. Growth rate inhibition metrics correct for confounders in measuring sensitivity to cancer drugs. Nature Methods. 2016;13(6):521-7. doi: 10.1038/nmeth.3853.
17. Ariey F, Witkowski B, Amaratunga C, Beghain J, Langlois AC, Khim N, Kim S, Duru V, Bouchier C, Ma L, Lim P, Leang R, Duong S, Sreng S, Suon S, Chuor CM, Bout DM, Ménard S, Rogers WO, Genton B, Fandeur T, Miotto O, Ringwald P, Le Bras J, Berry A, Barale JC, Fairhurst RM, Benoit-Vical F, Mercereau-Puijalon O, Ménard D. A molecular marker of artemisinin-resistant Plasmodium falciparum malaria. Nature. 2014;505(7481):50-5. Epub 20131218. doi: 10.1038/nature12876. PubMed PMID: 24352242; PMCID: PMC5007947.
18. Straimer J, Gnädig NF, Witkowski B, Amaratunga C, Duru V, Ramadani AP, Dacheux M, Khim N, Zhang L, Lam S, Gregory PD, Urnov FD, Mercereau-Puijalon O, Benoit-Vical F, Fairhurst RM, Ménard D, Fidock DA. K13-propeller mutations confer artemisinin resistance in Plasmodium falciparum clinical isolates. Science. 2015;347(6220):428-31. doi: doi:10.1126/science.1260867.
19. Stewart LB, Escolar EL, Philpott J, Cox-Singh J, Singh B, Conway DJ. Intrinsic multiplication rate variation of Plasmodium falciparum in clinical isolates prior to elimination in Malaysia. International Journal for Parasitology. 2025. doi: https://doi.org/10.1016/j.ijpara.2025.02.003.
20. Behrens Hannah M, Schmidt S, Henshall Isabelle G, López-Barona P, Peigney D, Sabitzki R, May J, Maïga-Ascofaré O, Spielmann T. Impact of different mutations on Kelch13 protein levels, ART resistance, and fitness cost in Plasmodium falciparum parasites. mBio. 2024;15(6):e01981-23. doi: 10.1128/mbio.01981-23.
21. Association of mutations in the Plasmodium falciparum Kelch13 gene (Pf3D7_1343700) with parasite clearance rates after artemisinin-based treatments-a WWARN individual patient data meta-analysis. BMC Med. 2019;17(1):1. Epub 20190117. doi: 10.1186/s12916-018-1207-3. PubMed PMID: 30651111; PMCID: PMC6335805.
22. Looareesuwan S, Kyle DE, Viravan C, Vanijanonta S, Wilairatana P, Charoenlarp P, Canfield CJ, Webster HK. Treatment of patients with recrudescent falciparum malaria with a sequential combination of artesunate and mefloquine. Am J Trop Med Hyg. 1992;47(6):794-9. doi: 10.4269/ajtmh.1992.47.794. PubMed PMID: 1471736.

23. Hott A, Casandra D, Sparks KN, Morton LC, Castanares GG, Rutter A, Kyle DE. Artemisinin-resistant Plasmodium falciparum parasites exhibit altered patterns of development in infected erythrocytes. Antimicrob Agents Chemother. 2015;59(6):3156-67. Epub 20150316. doi: 10.1128/aac.00197-15. PubMed PMID: 25779582; PMCID: PMC4432152.
24. Wang P, Read M, Sims PF, Hyde JE. Sulfadoxine resistance in the human malaria parasite Plasmodium falciparum is determined by mutations in dihydropteroate synthetase and an additional factor associated with folate utilization. Mol Microbiol. 1997;23(5):979-86. doi: 10.1046/j.1365-2958.1997.2821646.x. PubMed PMID: 9076734.
25. Teuscher F, Chen N, Kyle DE, Gatton ML, Cheng Q. Phenotypic changes in artemisinin-resistant Plasmodium falciparum lines in vitro: evidence for decreased sensitivity to dormancy and growth inhibition. Antimicrob Agents Chemother. 2012;56(1):428-31. Epub 20111010. doi: 10.1128/aac.05456-11. PubMed PMID: 21986828; PMCID: PMC3256014.
26. Kümpornsin K, Kochakarn T, Yeo T, Okombo J, Luth MR, Hoshizaki J, Rawat M, Pearson RD, Schindler KA, Mok S, Park H, Uhlemann A-C, Jana GP, Maity BC, Laleu B, Chenu E, Duffy J, Moliner Cubel S, Franco V, Gomez-Lorenzo MG, Gamo FJ, Winzeler EA, Fidock DA, Chookajorn T, Lee MCS. Generation of a mutator parasite to drive resistome discovery in Plasmodium falciparum. Nature Communications. 2023;14(1):3059. doi: 10.1038/s41467-023-38774-1.
27. Gnädig NF, Stokes BH, Edwards RL, Kalantarov GF, Heimsch KC, Kuderjavy M, Crane A, Lee MCS, Straimer J, Becker K, Trakht IN, Odom John AR, Mok S, Fidock DA. Insights into the intracellular localization, protein associations and artemisinin resistance properties of Plasmodium falciparum K13. PLOS Pathogens. 2020;16(4):e1008482. doi: 10.1371/journal.ppat.1008482.
28. RIVADENEIRA EM, WASSERMAN M, ESPINAL CT. Separation and Concentration of Schizonts of Plasmodium falciparum by Percoll Gradients. The Journal of Protozoology. 1983;30(2):367-70. doi: https://doi.org/10.1111/j.1550-7408.1983.tb02932.x.
29. Lambros C, Vanderberg JP. Synchronization of Plasmodium falciparum erythrocytic stages in culture. J Parasitol. 1979;65(3):418-20. PubMed PMID: 383936.
30. Duchon CE. Lanczos Filtering in One and Two Dimensions. Journal of Applied Meteorology and Climatology. 1979;18(8):1016-22. doi: https://doi.org/10.1175/1520-0450(1979)018<1016:LFIOAT>2.0.CO;2.
31. Ronneberger O, Fischer, P. & Brox, T. U-net: convolutional networks for biomedical image segmentation. In Proc. 18th International Conference on Medical Image Computing and Computer-Assisted Intervention (eds Navab, N. et al.) 234–241. Springer. 2015.
32. Agarap AF. Deep Learning using Rectified Linear Units (ReLU). Preprint at https://arxivorg/abs/180308375 (2018). 2018.
33. Diederik P. Kingma JB. Adam: A Method for Stochastic Optimization. Preprint at https://arxivorg/abs/14126980 (2014). 2014.

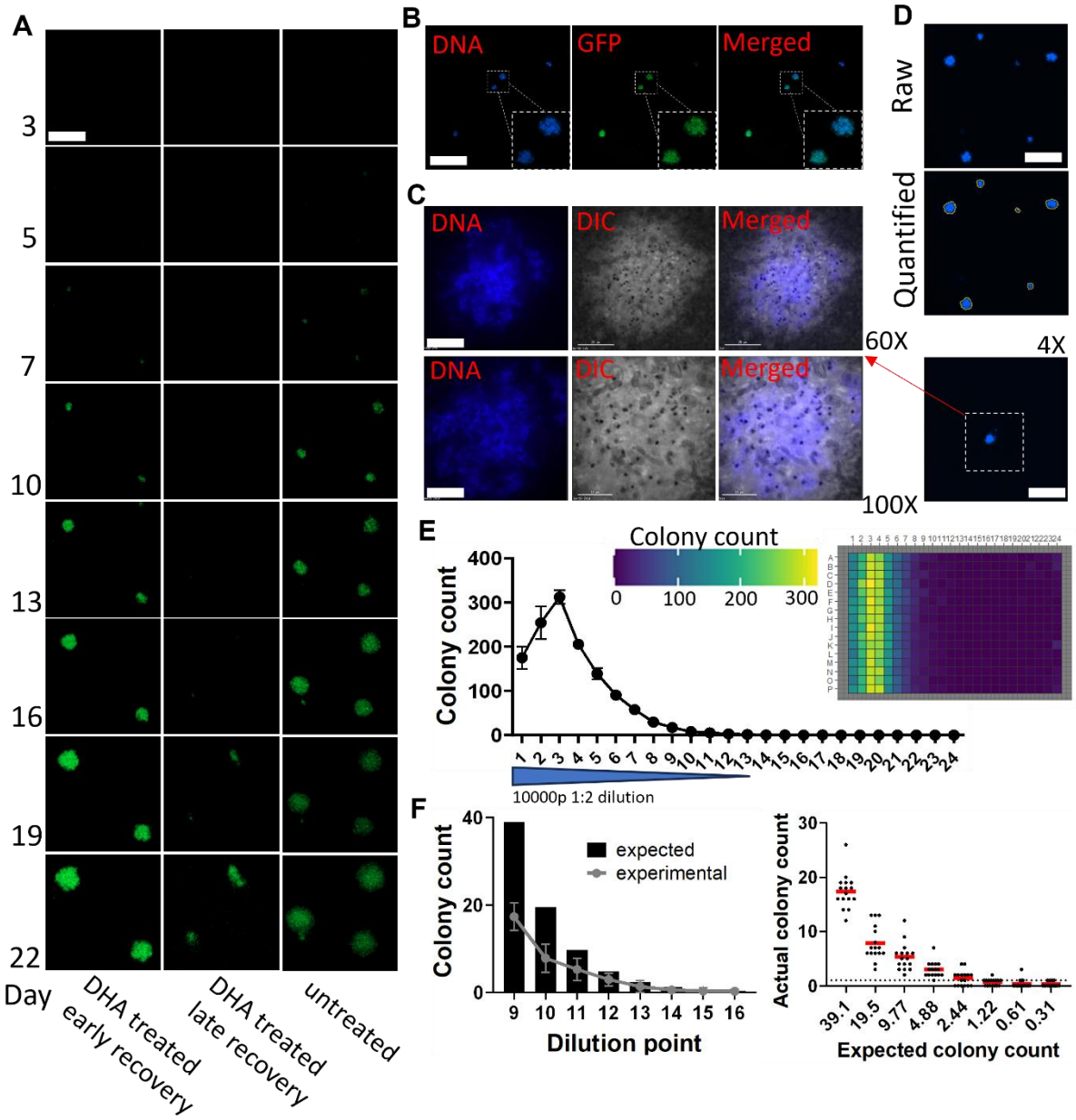

841

842

843

844

845

846

847 **Fig. 1. A single parasite grows into a colony. (A)** Growth of the same individual NF54-GFP
848 colonies imaged over time with or without 6h DHA exposure. Scale bar 150μm. **(B)** Hoechst and
849 GFP fluorescent images of day 7 parasite colonies imaged with a 4x objective, white boxes
850 show the same colonies imaged with a 20X objective. Scale bar 100μm. **(C)** Higher
851 magnification images of a day 7 parasite colony. The observed black dots are hemozoin. Top:
852 imaged with a 60X objective, scale bar 25μm, bottom: imaged with a 100X objective, scale bar
853 15μm. 4X objective image scale bar 100μm. **(D)** High-content image analysis used to measure
854 the number and the size of colonies of a fraction of a well (Full well is shown in Fig. S1C). Scale
855 bar 100μm. **(E)** Average number of colonies in each column of each dilution point (left) and
856 heatmap view of colony counts of the same serial dilution plate (right). Points 1 and 2 could not
857 be accurately quantified due to wells having too many colonies. **(F)** Comparison between
858 experimental results and estimated numbers in low dilution points (left) and comparison of the
859 number of colonies between quantified and expected (right). The estimated colony numbers are
860 shown in Fig. S3A. All experiments were performed at least twice.

861

862

863

864

865

866

867

868

869

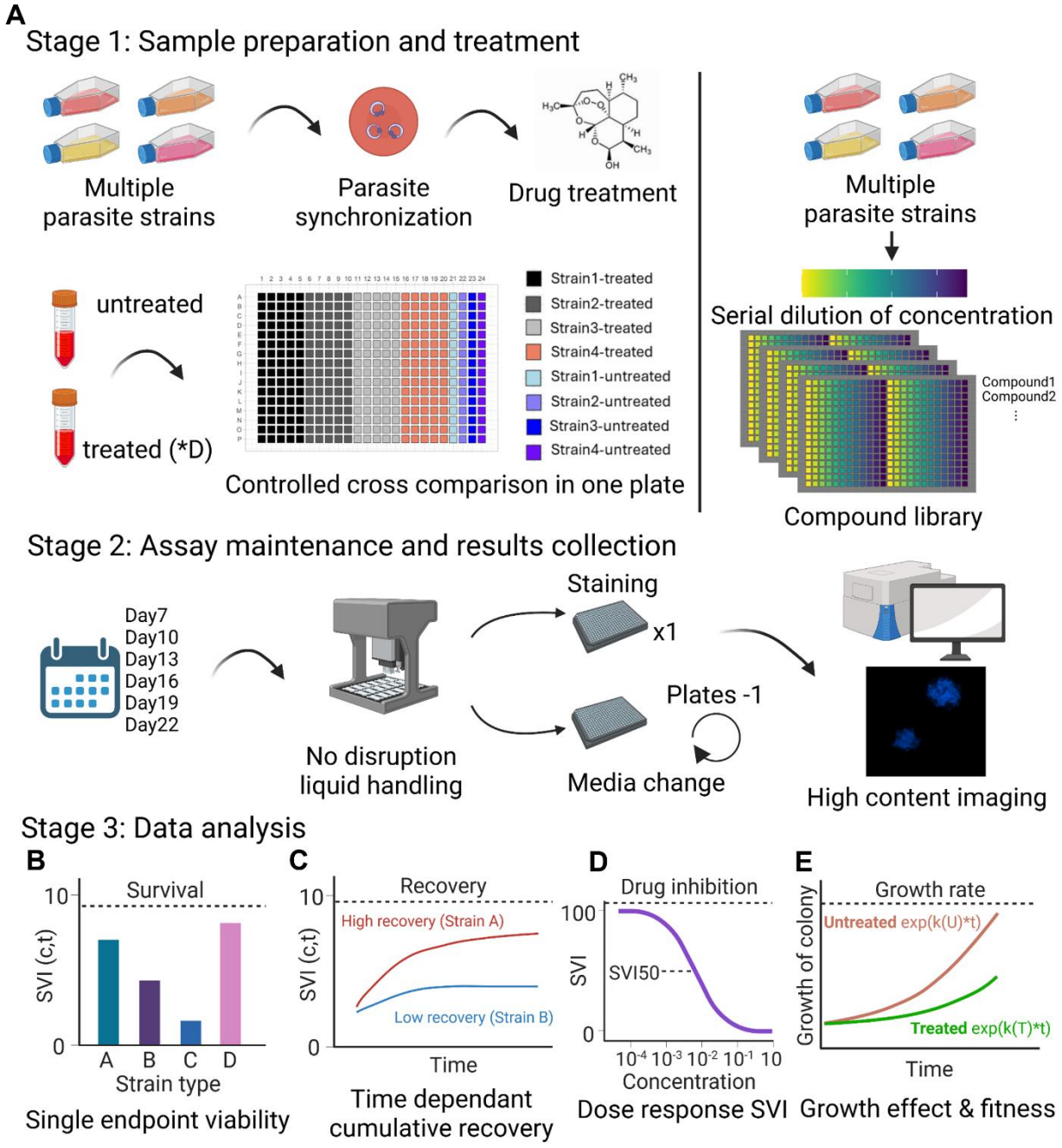

870

871

872

873

874

875 **Fig. 2. qTRACE reports viability, time-dependent recovery, and growth effects at single**
876 **parasite resolution. (A)** Schematics of the qTRACE process. In stage 1, parasite strains are
877 prepared and treated with drugs. Treated and untreated samples are prepared based on the
878 dilution factor D, then plated on the same plate. Left side showing representative DHA exposure
879 workflow and right side showing representative drug testing workflow. In stage 2, plates undergo
880 automated media change, and one plate is taken for HCI at each designated timepoint. In Stage
881 3, data are analyzed as described in Fig. 2B-E. **(B)** Single endpoint SVI assessments to
882 evaluate percentage viability at concentration c and time t. **(C)** Assessments of SVI at multiple
883 time points to evaluate time-dependent recovery or drug effects. **(D)** SVI assessments in a dose
884 response. SVI50 is the concentration of a drug that incurs 50% viability. **(E)** Assessments of
885 exponential growth of colonies under different conditions or between different strains to evaluate
886 growth effects and fitness. GR is then derived using variable K between two conditions.

887

888

889

890

891

892

893

894

895

896

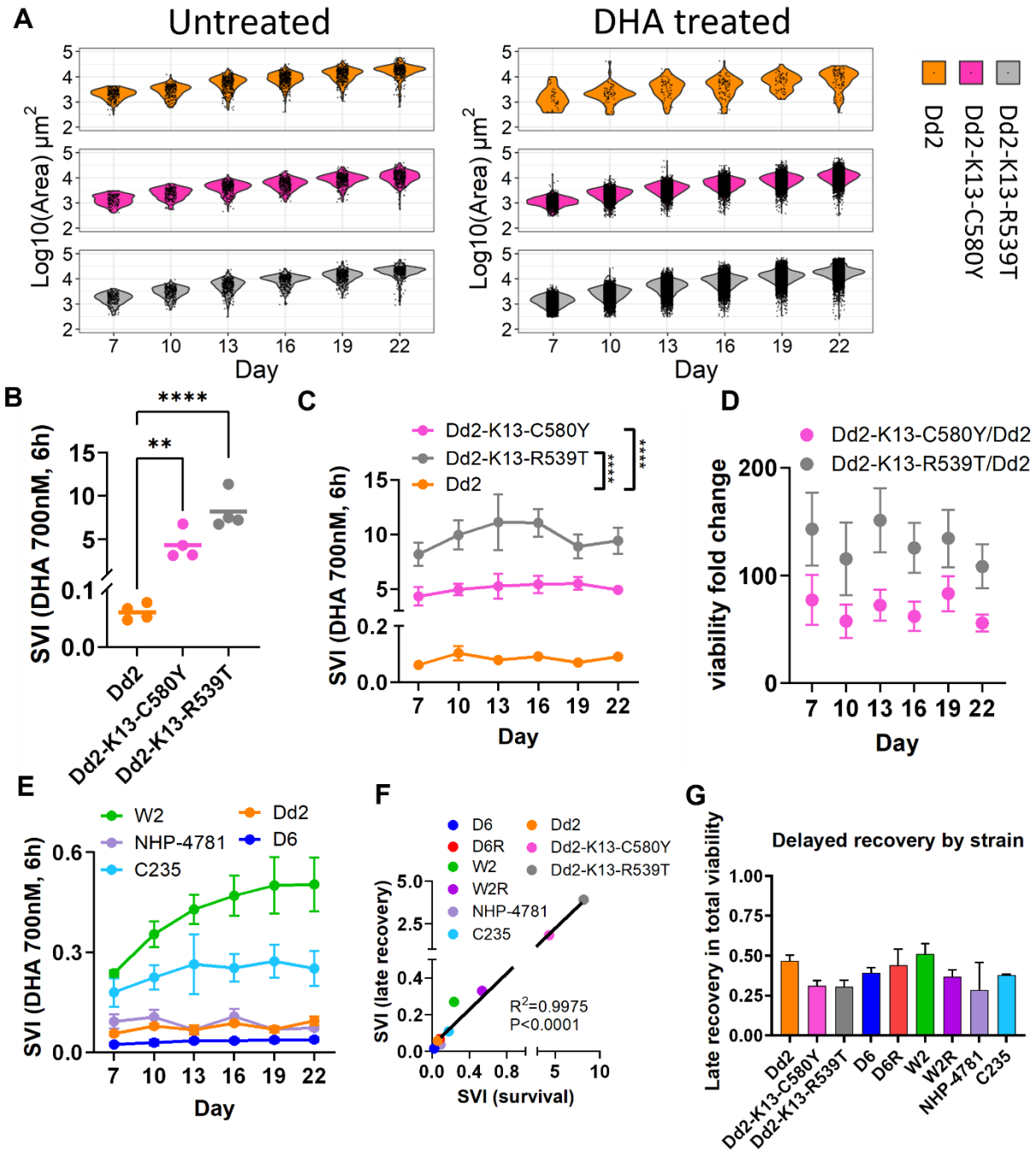

897

898

899

900

901 **Fig. 3. qTRACE reveals differential susceptibility and recovery to DHA exposure across**
902 **various parasite lines. (A)** Individual colonies and the sizes of each colony under untreated
903 condition (left) and DHA condition (right) for every timepoints of Dd2 and Dd2 K13 mutants.
904 Every black dot represents one colony. From two biological replicates. **(B)** SVI assessment of
905 Dd2 and Dd2 K13 mutants on day 7 initial survival from DHA exposure, n=80 technical replicate
906 (TR) and n=4 biological replicates (BR). **(C)** Time-dependent SVI of Dd2 and Dd2 K13 mutants
907 at continuous timepoints, day 19 and 22 for Dd2-K13-R539T were not accurately quantified due
908 to colony overgrowth. n=80 TR and n=4 BR. **(D)** The fold change in SVI between Dd2 and Dd2-
909 K13-C580Y, as well as between Dd2 and Dd2-K13-R539T, for all timepoints. **(E)** Time
910 dependent recovery SVI of five artemisinin sensitive strains at continuous timepoints n=80 TR
911 and n=3 BR. **(F)** Comparison of late recovery SVI (Max SVI-survival SVI) and survival SVI of all
912 nine parasite lines with linear regression. P-value and R^2 value calculated using Pearson's
913 correlation. **(G)** Proportion of late recovery in total viability over 22 days across nine parasite
914 lines (error bar=SEM). More data in Supplementary Table 1.

915

916

917

918

919

920

921

922

923

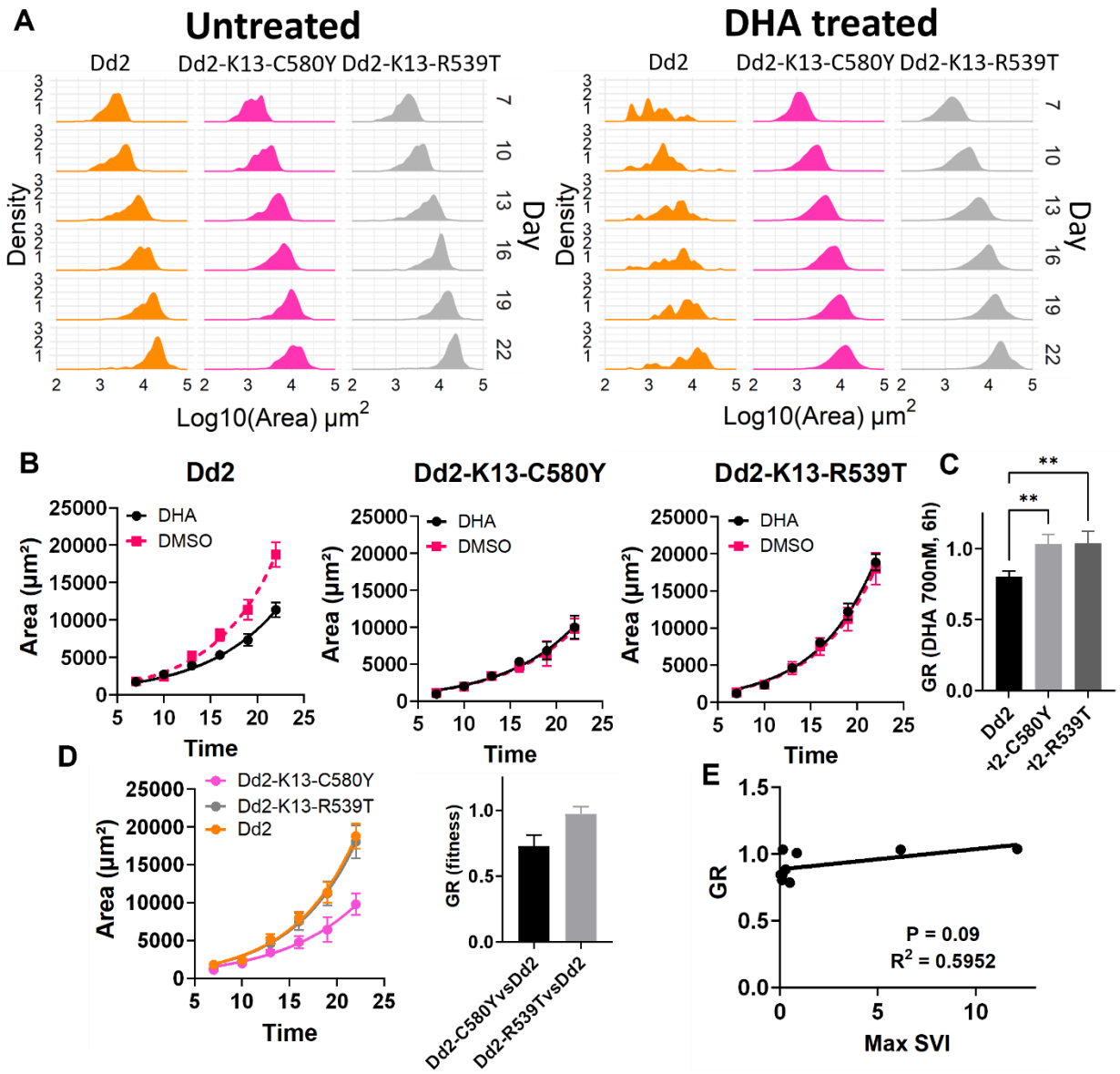

924

925

926

927

928

929

930

931 **Fig. 4. Growth impacts induced by DHA and fitness costs to artemisinin resistance. (A)**
932 Density distribution of colony sizes in Dd2 and Dd2 K13 mutants at continuous timepoints in
933 DHA and DMSO condition. From two biological replicates. **(B)** Fitted growth curves of averaged
934 colony sizes at all timepoints for Dd2 (left), Dd2-K13-C580Y (middle), and Dd2-K13-R539T
935 (right) in DHA condition and DMSO condition. n=80 TR and n=4 BR. **(C)** GR values of Dd2 and
936 Dd2 K13 mutants comparing DHA condition to DMSO condition for each strain. **(D)** Fitted
937 growth curves of averaged colony sizes at all timepoints for Dd2 and Dd2 K13 mutants without
938 any treatment (left) and GR values between parasite lines (right). n=80 TR and n=4 BR. **(E)**
939 Correlation comparison between Max SVI and GR for all nine parasite lines tested with linear
940 regression. P-value and R^2 value calculated using Pearson's correlation. More data in
941 Supplementary Table 2.

942

943

944

945

946

947

948

949

950

951

952

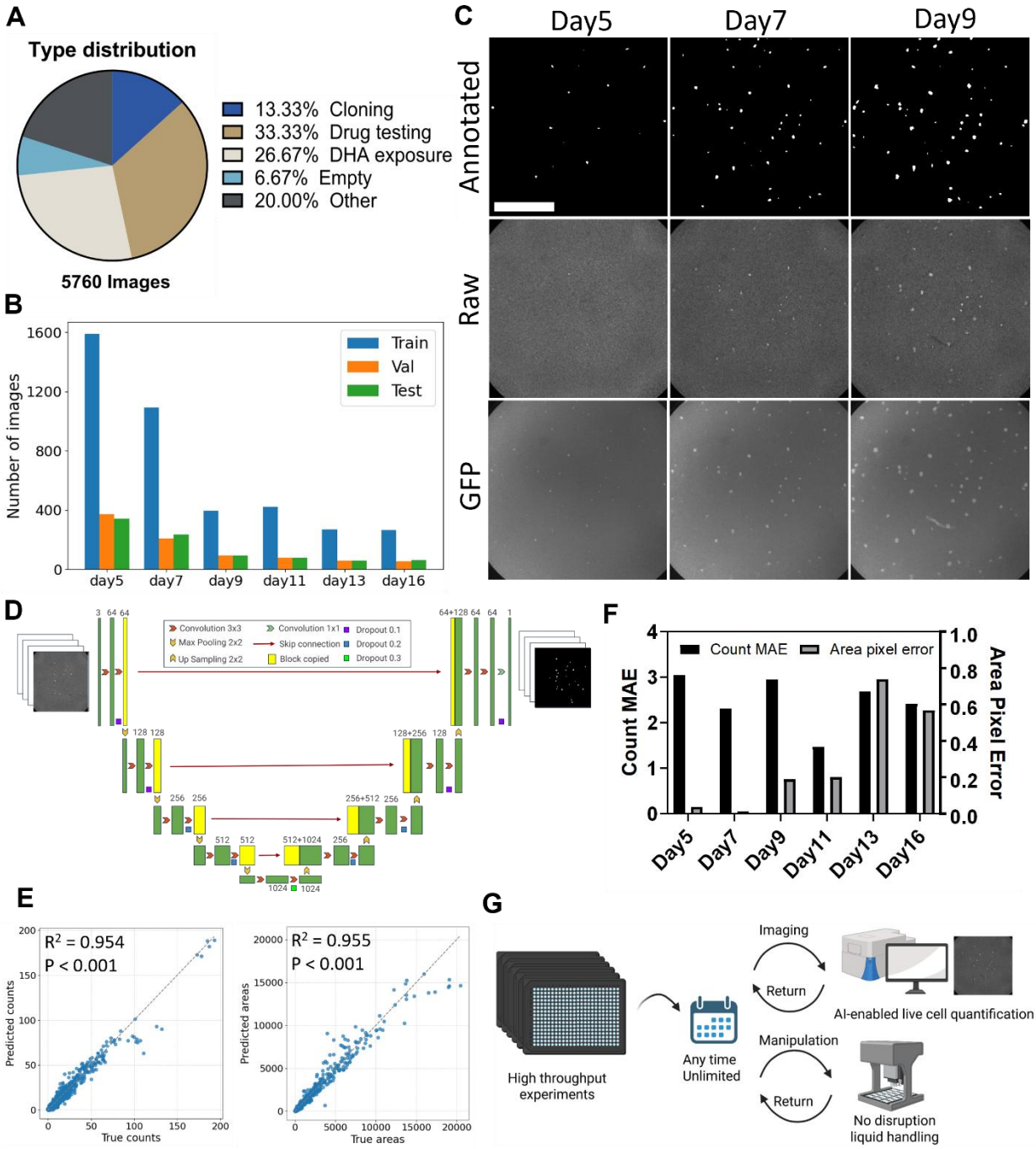
A
Type distribution
13.33% Cloning
33.33% Drug testing
26.67% DHA exposure
6.67% Empty
20.00% Other
5760 Images
B
Number of images
Train
Val
Test
day5
day7
day9
day11
day13
day16
C
Day5
Day7
Day9
Annotated
Raw
GFP
D
Convolution 3x3
Max Pooling 2x2
Up Sampling 2x2
Convolution 1x1
Skip connection
Block copied
Dropout 0.1
Dropout 0.2
Dropout 0.3
E
R^2 = 0.954
P < 0.001
Predicted counts
True counts
R^2 = 0.955
P < 0.001
Predicted areas
True areas
F
Count MAE
Area pixel error
Count MAE
Area Pixel Error
Day5
Day7
Day9
Day11
Day13
Day16
G
High throughput experiments
Any time Unlimited
Imaging
Return
AI-enabled live cell quantification
Manipulation
Return
No disruption liquid handling

957 **Fig. 5. Deep learning enables continuous label-free live cell analysis. (A)** Distribution of
958 training datasets by types of experiments. **(B)** Distribution of training datasets by timepoints and
959 training, validation and test. **(C)** Representative raw transmitted light images and human
960 annotated mask images for a continuous experiment. GFP was used as annotation reference to
961 confirm authenticity of colonies on transmitted light images. Scale bar 1000μm. **(D)** Schematics
962 of model architecture and qTRACE AI application. **(E)** Evaluation of model prediction accuracy
963 compared to human annotated results for count (left) and area (right). P-value and R^2 value
964 calculated using Pearson's correlation. **(F)** Count MAE and area pixel error percentage of the
965 trained model by timepoint. **(G)** Schematics showing qTRACE AI workflow. Unlimited imaging
966 and manipulation of same sample over time.

967

968

969

970

971

972

973

974

975

976

977

978

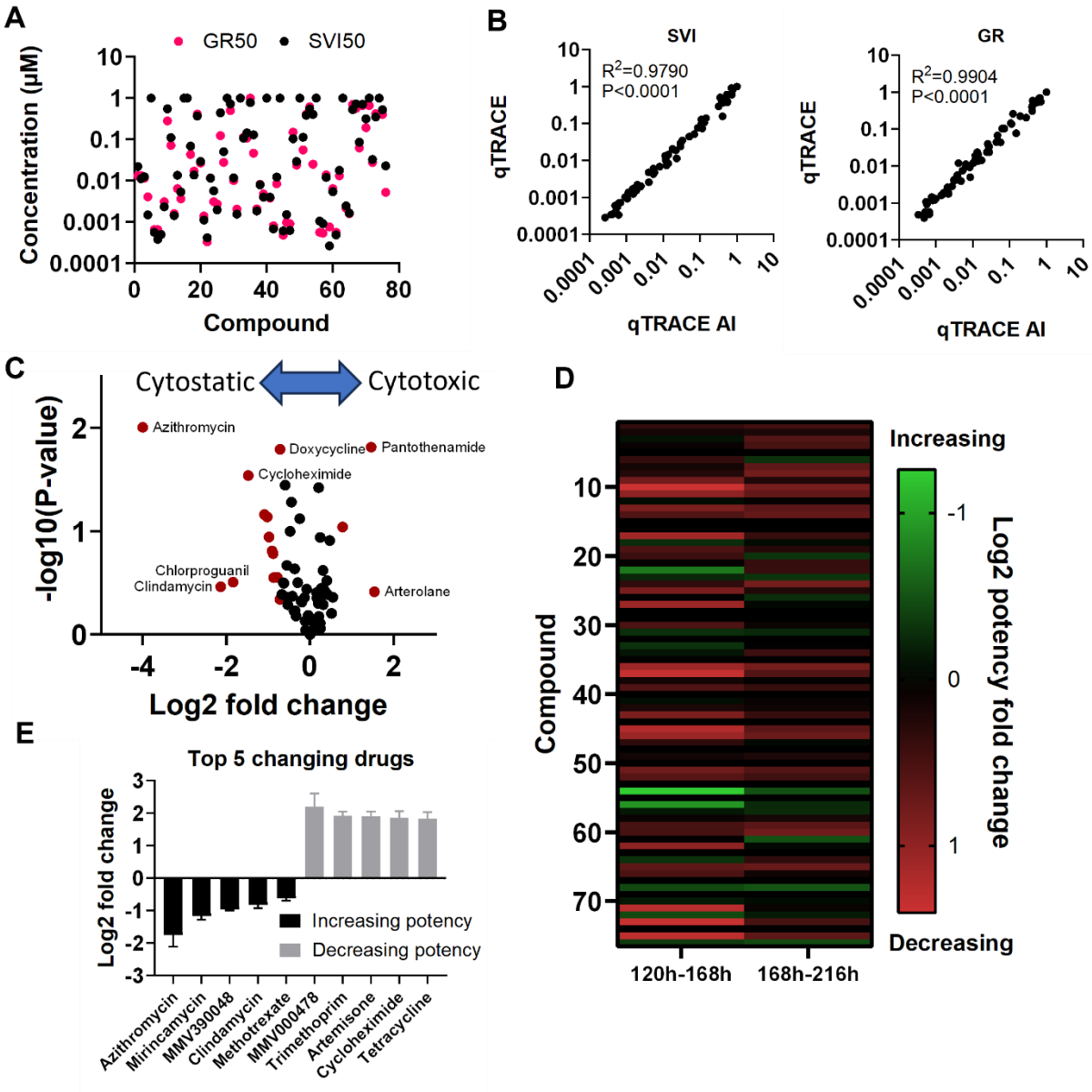

979

980

981

982

983

984

985 **Fig. 6. qTRACE reveals new insights into drug activities and effects. (A)** SVI50 and GR50
986 for drugs tested from MMV antimalarial reference library. n=2 BR. **(B)** Comparison of screening
987 results between qTRACE AI and qTRACE for SVI (left) and GR (right). P-value and R^2 value
988 calculated using Pearson's correlation. **(C)** Cytotoxic and cytostatic effect evaluation of drugs
989 from MMV antimalarial reference library. Shifting in directions represents preference of either
990 cytostatic effect (left) or cytotoxic effect (right). **(D)** Effect of altering time on SVI50 shift for drugs
991 from MMV antimalarial reference library at 48h interval. n=2 BR. **(E)** Top 5 drugs showing the
992 highest potency shift for each direction over entire measured time course. Error bar SEM.

993

994

995

996

997

998

999

1000

1001